Materials Science & Engineering A 858 (2022) 144136

Contents lists available at ScienceDirect

Materials Science & Engineering A

journal homepage: www.elsevier.com/locate/msea

Characterization of hot extrusion deformation behavior, texture evolution, and mechanical properties of Mg–5Li–3Sn–2Al–1Zn magnesium alloy

Yuhang Guo [a,*], Xuancheng He [a], Yibo Dai [a], Qianhao Zang [a], Xuguang Dong [b], Zhenya Zhang [c]

[a] School of Materials Science and Engineering, Jiangsu University of Science and Technology, Zhenjiang, 212003, China
[b] School of Materials Science and Engineering, Shenyang Ligong University, Shenyang, 110159, China
[c] School of Materials Science and Engineering, Jiangsu University, Zhenjiang, 212003, China

ARTICLE INFO

Keywords:
Mg-Li alloy
Extrusion
Microstructure
Mechanical properties
Dynamic recrystallization

ABSTRACT

The effects of four different hot extrusion processes on the microstructure, texture, and mechanical properties of Mg–5Li–3Sn–2Al–1Zn alloys were investigated with the help of optical microscope (OM), scanning electron microscope (SEM), transmission electron microscope (TEM) and electron backscatter diffraction (EBSD) techniques. The results show that the magnesium alloy experienced dynamic recrystallization during the hot extrusion processes, the grain size was significantly refined compared with that of the cast alloy, and the mechanical properties of the alloy were significantly improved. After the 105° forward-parallel channel extrusion process, the alloy exhibited optimal strength and plasticity with 178 MPa, 270 MPa, and 21.03% for tensile yield strength, ultimate tensile strength, and elongation, respectively, which were 61.8%, 44.4%, and 134.4% higher compared to the homogeneous state. The increase in strength is attributed to fine grain strengthening, while the significant increase in plasticity is due to the weakening of the basal texture and the improved coordination of plastic deformation of the magnesium alloy following grain refinement.

1. Introduction

Typically, the Mg–Li alloy is the lightest magnesium alloy, with a lower density than any other magnesium or aluminum alloy. It also has good plasticity and molding properties. Therefore, an Mg–Li-based alloy is expected to become a new ultralight magnesium alloy adapted to industrial production, further reducing carbon emissions and achieving carbon neutrality and carbon peaking [1–3]. However, the extremely poor room temperature strength of Mg–Li alloys limits their industrial application [4–6]. Generally, adding appropriate amounts of alloying elements effectively improves the mechanical properties of materials and typical strengthening elements, such as Al, Zn, Mn, and REs [7–11]. In addition, Li can affect the mechanical properties of magnesium by changing its crystal structure. The phase structure of the Mg–Li alloy can also be influenced by the Li content: when the Li content is below 5.7 wt %, the Mg–Li alloy has an α-Mg single-phase structure; when the Li content is between 5.7 wt% and 10.3 wt%, the Mg–Li alloy has an α-Mg and β-Li dual-phase structure; and when the Li content is above 10.3 wt %, the Mg–Li alloy has a β-Li single-phase structure [12–15]. Al has a strong solid solution strengthening effect and is among the most important additive elements [16,17]. Zn can improve the strength and plasticity of magnesium alloys by refining its grain size [18,19]. Sn can also improve the strength of magnesium alloys: the addition of Sn can form Mg_2Sn and Li_2MgSn in the magnesium matrix, which will participate in preventing dislocation movement, thereby improving the mechanical properties of the alloy [12]. Meanwhile, increasing the melting point of the formed Mg_2Sn precipitates will improve the mechanical properties of the Mg–Li alloy at high temperatures [20].

The methods of improving the mechanical properties of Mg–Li alloys are not limited to alloying additions. Thermomechanical processes have also been shown to be imperative in improving mechanical properties through microstructural refinement [21]. The hot extrusion process has an excellent grain refinement effect, and the Hall–Petch relationship states that grain refinement can enhance the tensile strength of the alloy [22]. The hot extrusion process also significantly affected the texture of Mg–Li alloys [23]. Many materials researchers have reported on the effects of hot extrusion on the mechanical properties of Mg–Li-based alloys. Son et al. [24] found that adding Li to an Mg–3Zn–1Sn-0.4Mn-based alloy formed $MgLi_2Sn$ precipitates, which are imperative in improving the mechanical properties of the alloy. With an increase in Li, the plasticity of the alloy was greatly enhanced. When 8% Li was added, the elongation (EL) was 49.3%, but the ultimate

* Corresponding author.
E-mail addresses: guoyuhang@just.edu.cn, guoyuhang@126.com (Y. Guo).

https://doi.org/10.1016/j.msea.2022.144136
Received 25 August 2022; Received in revised form 29 September 2022; Accepted 30 September 2022
Available online 5 October 2022

tensile strength dropped to 147 MPa. Tang et al. [25] also found that the Li content strongly influenced the plasticity of the Mg-xLi-3Al–2Zn-0.2Y (x = 5, 8, 11) alloy. Shear bands were observed in the as-extruded Mg–5Li–3Al–2Zn-0.2Y but not in the other two extruded alloys, suggesting that the plasticity of the alloy significantly increased with an increased Li content. In addition, the behavior of solid solution strengthening during annealing was observed in other alloys with high Li content. Pugazhendhi et al. [26] found that β-Li effectively enhances the plasticity of Mg–Li alloys and that the solute effect of Al is crucial in improving the strength of the Mg–8Li alloy. The Mg–8Li–6Al alloy showed a maximum tensile yield strength and ultimate tensile strength of 192 MPa and 250 MPa, respectively. Chang et al. [27] reported the effect of Sn and Y on the mechanical properties of the Mg–9Li–3Al alloy. They found that adding Sn improves the strength of the alloy due to grain refining and precipitation strengthening, while Y promotes the pyramidal <a + c> slip in the α-phase and the volume fraction of the β-phase, thus improving the ductility of the Mg–9Li–3Al alloy.

Reviewing previous studies on Mg–Li alloys [24–27], two main issues have limited the large-scale industrial application of Mg–Li alloys: first, the Mg–Li-based alloys they prepared had high Li content; second, the extrusion ratio of their Mg–Li-based alloys was high. The first issue greatly increases the production cost of Mg–Li alloys [28]. Moreover, a high extrusion ratio is demanding on the extrusion equipment and reduces their mold life, further limiting the large-scale application of high-strength Mg–Li-based alloys in the industry. In addition, there are few studies on the effect of the magnesium alloy one-pass forming process on the mechanical properties of Mg–Li-based alloys. To explore the effect of the one-step extrusion process on the mechanical properties of Mg–Li-based alloys, a low-alloyed Mg–5Li–3Sn–2Al–1Zn alloy was prepared in this work. The Mg–5Li–3Sn–2Al–1Zn alloy was applied to Φ12 forward extrusion (Φ12 FE), Φ10 forward extrusion (Φ10 FE), 90° forward-parallel channel extrusion (90° FPE), and 105° forward-parallel channel extrusion (105° FPE). The effect of the hot extrusion process on the grain structure and dynamic recrystallization behavior of magnesium alloys was shown by the microstructural changes. Moreover, tensile tests at room temperature were performed on extruded specimens for each process to illustrate the effect of these microstructural changes on the strength and plasticity of the alloy. This provides an effective approach to commercializing large structural pieces of Mg–Li-based alloys.

2. Materials and methods

The Mg–5Li–3Sn–2Al–1Zn alloy used in this work was prepared using pure Sn (99.95 wt%), pure Al (99.95 wt%), pure Zn (99.90 wt%), and Mg–13Li master alloy. The above metal raw materials were melted in a vacuum induction melting furnace under a protective atmosphere of high-purity Ar. The liquid alloy was poured into a cylindrical steel mold preheated to 150 °C and cooled naturally to room temperature to obtain the original ingot, with a size of Φ90 × 220 mm. The actual composition of the alloy was tested using inductivity-coupled plasma atomic emission spectroscopy (ICP-AES). The results are shown in Table 1. The heat-treated specimens were sampled in the equiaxial crystal zone, with a size of Φ20.5 × 140 mm. To prevent oxidation or combustion of the specimen during heat treatment, the specimens were sealed in a glass tube and evacuated with a vacuum of 1×10^{-2} Pa. The heat-treated specimens were homogenized at 400 °C for 24 h and water-cooled. Subsequently, the specimens were machined to remove the oxide skin and were split into Φ20 × 40 mm for hot extrusion. Hot extrusion processes were conducted at 250 °C at an extrusion rate of 2 mm/s. Four hot extrusion processes are shown in Fig. 1(a).

Table 1
Chemical composition of the Mg–5Li–3Sn–2Al–1Zn alloy (wt.%).

Alloy	Mg	Sn	Al	Zn	Li
Mg–5Li–3Sn–2Al–1Zn	Bal.	3.17	2.07	1.08	5.23

The phase and macrotexture analyses were identified using X-Ray Diffraction (XRD, D8 advance). The target material was Cu (λ = 1.5418Å), the operating voltage was 40 kV, and the operating current was 40 mA. XRD patterns of the phases were collected at diffraction angles from 20° to 80°, and the obtained data were analyzed using Jade 6.0. Macrotexture was analyzed using the reflection method on the basal plane (0001) and prismatic plane ($10\bar{1}0$) with measurement angles from 0° to 70°, and the obtained data were analyzed using Jtex. The microstructure was observed using an optical microscope (OM, VHX-900), a transmission electron microscope (TEM, JEOL-2100 F), and a scanning electron microscope (SEM, JSM-7900F) equipped with an energy dispersive spectrometer (EDS) and an electron backscatter diffraction (EBSD) system. The data measured in the EBSD test were analyzed by Channel 5. The test surfaces for the XRD, OM, TEM, and EBSD analyses are shown in Fig. 1(b), where ED indicates the extrusion direction, TD indicates the transverse direction, and ND indicates the normal direction. Tensile tests at room temperature were conducted on a SANS universal testing machine with a displacement speed of 1 mm/min, and the tensile specimen size was 8 × 60 mm. At least three identical tests were performed for each alloy, and the average values were obtained. After the tensile tests, the fracture morphologies were observed and analyzed using an SEM (JSM-7900F).

3. Results

3.1. Microstructure

Fig. 2 shows the XRD patterns of the Mg–5Li–3Sn–2Al–1Zn alloy after the homogenizing heat treatment and hot extrusion processes. Diffraction peaks of the $\alpha - Mg$ phases were detected in all samples,

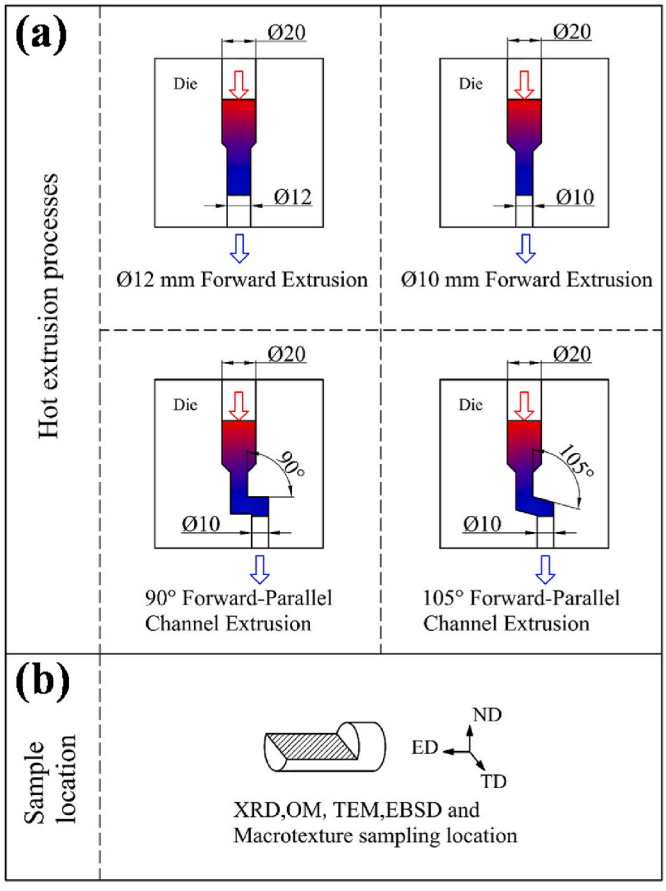

Fig. 1. Hot extrusion processes and sampling diagram.

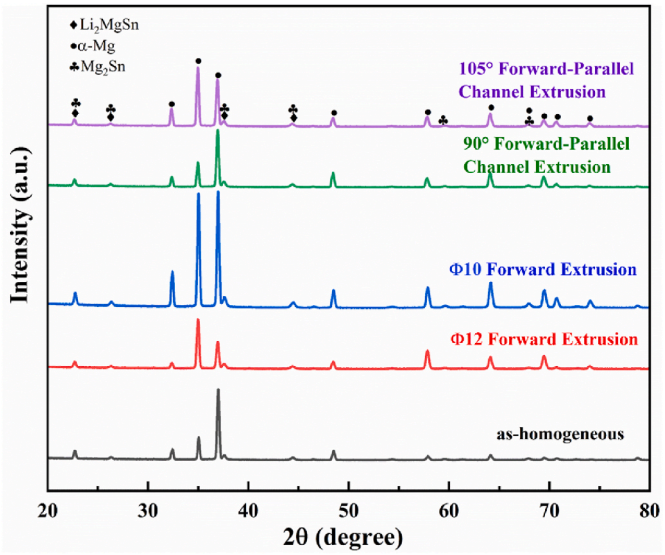

Fig. 2. XRD pattern of the alloys after hot treatment and hot extrusion processes.

while no diffraction peaks of the $\beta-$ Li phases were detected, consistent with the Mg–Li binary diagram. Other diffraction peaks correspond to the Mg_2Sn and Li_2MgSn phases. By comparing the as-homogeneous alloy with the as-extruded alloy, the intensity of the diffraction peaks at a 35° diffraction angle in the XRD pattern is shown to be significantly enhanced after the FE processes, indicating that the FE processes change the grain orientation of the alloy and that the basal texture is significantly enhanced. The intensity of the diffraction peak at the 35° diffraction angle was reduced for the alloys after two different FPE processes, indicating that the two additional passes of shear deformation further weakened the basal texture of the alloy. The intensity of the diffraction peak of the magnesium alloy at the 35° diffraction angle after 105° FPE is greater than that of the 90° FPE, indicating that the degree of shear deformation also affects the basal texture intensity of the Mg–5Li–3Sn–2Al–1Zn alloy.

Fig. 3 shows the SEM secondary electron images and the EDS results of the corresponding points of the Mg–5Li–3Sn–2Al–1Zn alloy after the homogenization heat treatment and hot extrusion processes. After homogenization, several bright precipitated phases appeared in the α-Mg matrix (Fig. 3(a)). We selected two typical locations for EDS analysis, and although both Points 1 (P1) and 2 (P2) were enriched with Mg and Sn, they had different shapes. Point 1 is a fine bar-like precipitation phase, and the EDS results show that the ratio of Mg to Sn is approximately 1:1. Since Li is undetectable by EDS analysis, combined with the analysis of the XRD results, the bar-like precipitation phase is Li_2MgSn. While Point 2 is a small white particle, the EDS results show that the ratio of Mg to Sn at this point is approximately 2:1, indicating that the precipitated phase may be Mg_2Sn. After different hot extrusion processes, the precipitated phases underwent different degrees of fragmentation and were uniformly distributed within the Mg matrix (Fig. 3 (b–e)). Two typical locations were selected for EDS analysis for each bright area after hot extrusion, and the results are shown in Fig. 3(f). We determined that the main composition of the precipitated phases in the bright areas was unchanged after hot extrusion, and the bar-like and particle-precipitated phases were Li_2MgSn and Mg_2Sn, respectively. The quantity of the bar-like phases decreased after hot extrusion, indicating that the Li_2MgSn phase was crushed during hot extrusion. Fu et al. [8] concluded that Li_2MgSn is a metastable phase, which is rapidly transformed into Mg_2Sn during hot extrusion.

Fig. 4 shows the optical micrographs of the Mg–5Li–3Sn–2Al–1Zn alloy after the hot extrusion processes and the corresponding average grain statistics. Fig. 4(a) and (b) show that some grains in the alloy experienced dynamic recrystallization during the FE process. However, coarse original grains remained, and their structure was not uniform. The average grain size was 5.03 μm and 4.86 μm. Comparing the two FPE processes, we found that the area fraction of DRXed grains in the alloy increased gradually after increasing the extrusion ratio [29]. Hence, the degree of dynamic recrystallization of the alloy is increased after the Φ10 FE process. During extrusion, the coarse original grains were elongated along the ED. Thus, Fig. 4(a) and (b) show that many

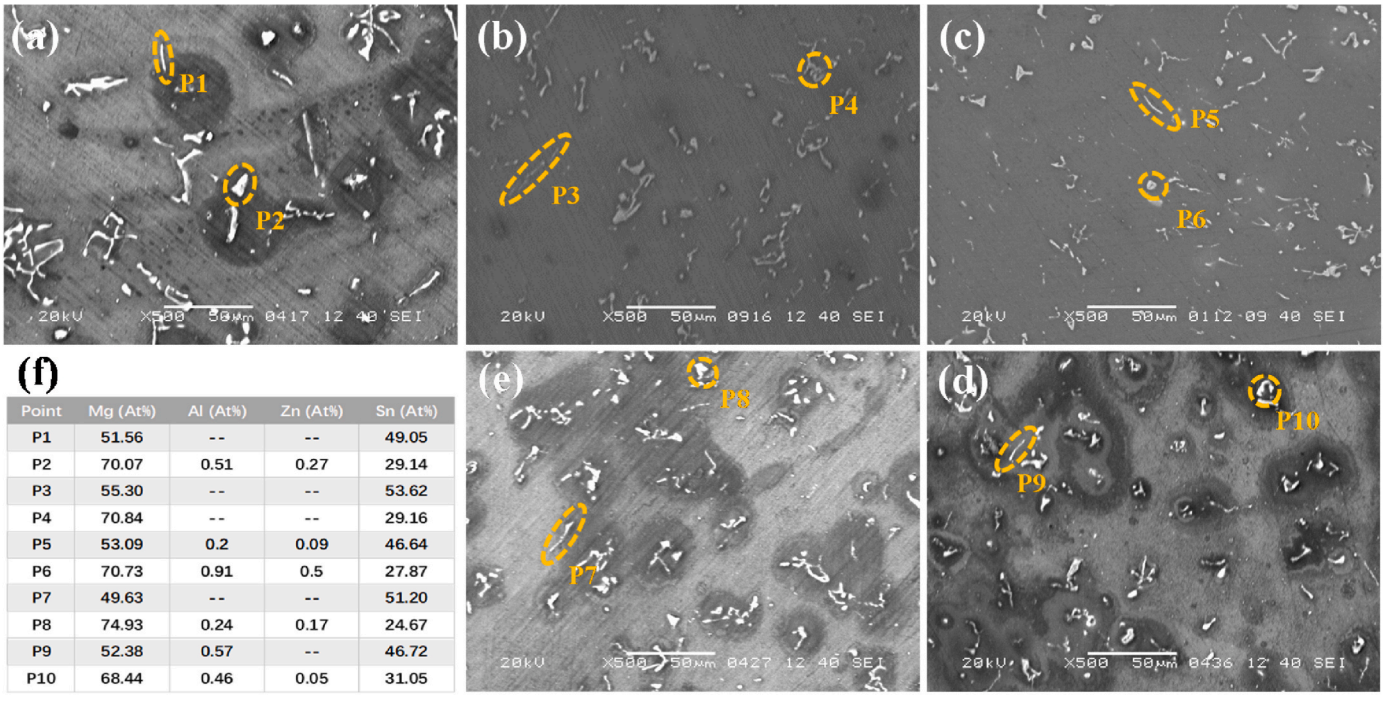

(f)

Point	Mg (At%)	Al (At%)	Zn (At%)	Sn (At%)
P1	51.56	--	--	49.05
P2	70.07	0.51	0.27	29.14
P3	55.30	--	--	53.62
P4	70.84	--	--	29.16
P5	53.09	0.2	0.09	46.64
P6	70.73	0.91	0.5	27.87
P7	49.63	--	--	51.20
P8	74.93	0.24	0.17	24.67
P9	52.38	0.57	--	46.72
P10	68.44	0.46	0.05	31.05

Fig. 3. SEM images and EDS results of the alloys after hot treatment and hot extrusion processes: (a) as-homogeneous, (b) Φ12 FE, (c) Φ10 FE, (d) 90° FPE, and (e) 105° FPE images and (f) EDS results.

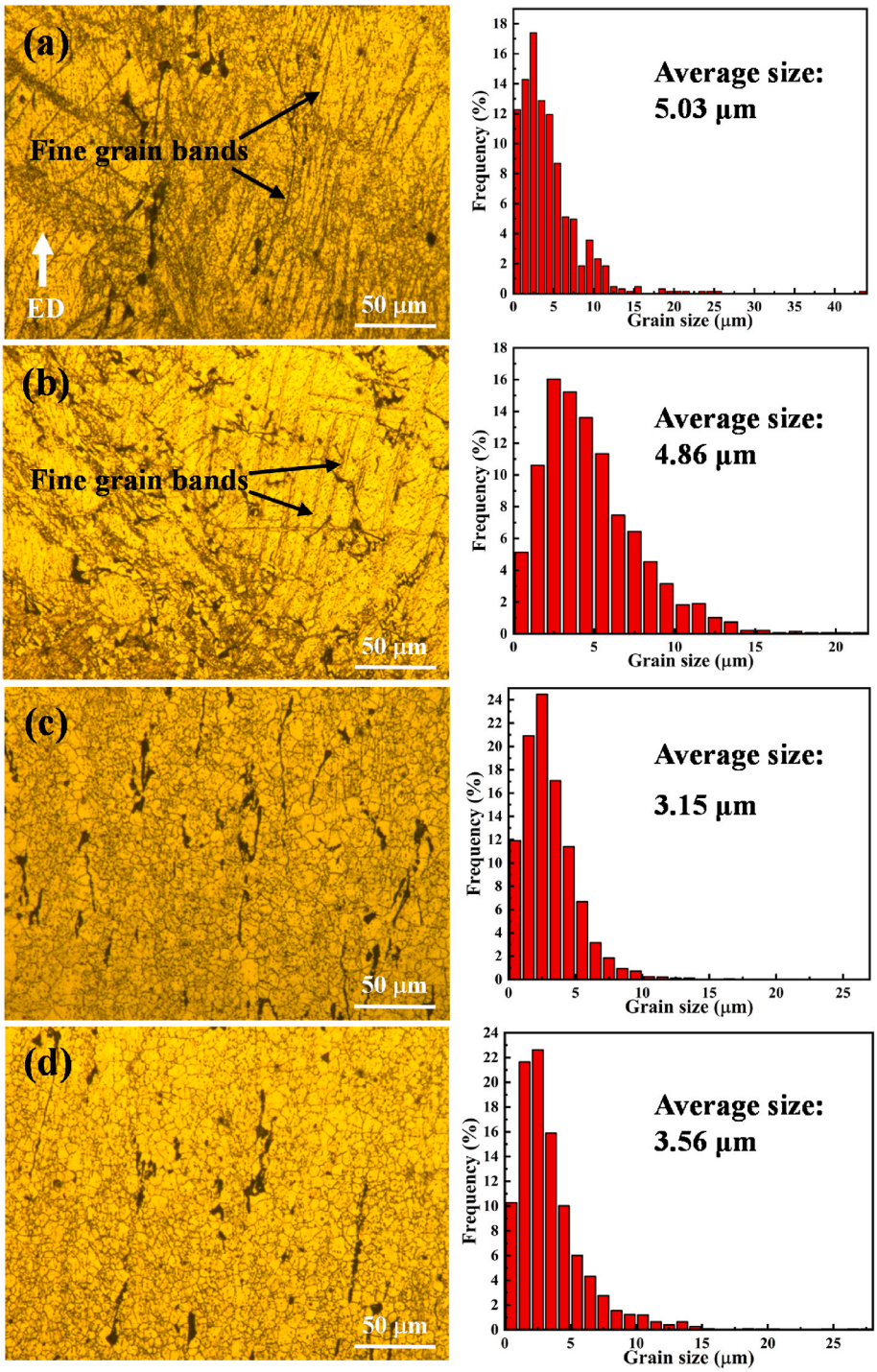

Fig. 4. Optical micrographs and statistical results of the grain size of the alloys after hot extrusion processes: (a) Φ12 FE, (b) Φ10 FE, (c) 90° FPE, and (d) 105° FPE.

fine grain bands parallel to the ED were distributed around the coarse original grains, exhibiting a typical bimodal structure. As shown in Fig. 4 (c) and (d), the microstructure was dominated by fine equiaxed grains after the FPE processes. Simultaneously, the structure had increased uniformity, which is effective in improving the plastic deformation properties of the alloy. In addition, the average grain size is further refined compared to the FE processes, which are 3.15 μm and 3.56 μm.

3.2. Mechanical properties

Fig. 5(a) shows the tensile stress–strain curves at room temperature for the as-homogeneous and as-extruded Mg–5Li–3Sn–2Al–1Zn alloys. The corresponding values of tensile yield strength (TYS), ultimate tensile strength (UTS), and elongation (EL) are shown in Table 2. In order to compare the effects of each extrusion process on the alloy properties, a comparative graph of the mechanical properties was plotted (Fig. 5(b)). The relative changes after each extrusion process compared to the as-homogeneous alloy are also shown in Fig. 5(b). The strength and plasticity of the alloy after the hot extrusion processes are much higher than those of the as-homogeneous alloy (Fig. 5(a)). This confirms that the thermomechanical processes have an over 50% stronger strengthening effect on the alloy—with YTS approximately 180 MPa, UTS above 250

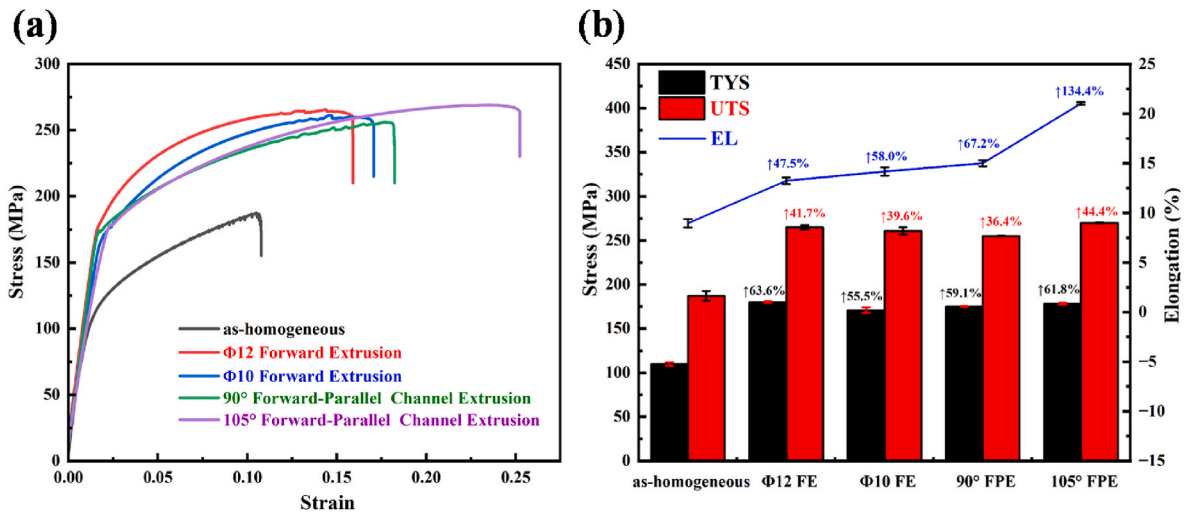

Fig. 5. Tensile properties of the alloy samples after hot treatment and hot extrusion processes.
(a) stress–strain curves and (b) comparison of mechanical properties.

Table 2
Tensile properties of the alloy samples after hot treatment and hot extrusion processes.

Processes	TYS (MPa)	UTS (MPa)	EL (%)
as-homogeneous	110	187	8.97
Φ12 FE	180	265	13.23
Φ10 FE	171	261	14.17
90° FPE	175	255	15
105° FPE	178	270	21.03

MPa, and a significant improvement in EL without loss of strength—compared to the as-homogeneous alloy.

4. Discussion

4.1. Microstructural evolution during different extrusion processes

EBSD tests were conducted to accurately analyze the microstructure evolution of Mg–5Li–3Sn–2Al–1Zn during the hot extrusion processes. Fig. 6 shows the grain orientation maps of the Mg–5Li–3Sn–2Al–1Zn alloy after the hot extrusion processes, and the different colors of the grains in the diagram represent different grain orientations [30,31]. In Fig. 6(a), most of the original grains with larger sizes exhibit a green color, indicating that their $<\bar{1}2\bar{1}0>\|$ED-preferred orientation was obvious. Meanwhile, some fine DRXed grains exhibit a red color, indicating that their orientation has changed significantly from that of the original grains, mostly $<0001>\|$ED-preferred orientation. The change in grain size and orientation indicates that the alloy experienced dynamic recrystallization after the Φ12 FE process, which increased the intensity of the basal texture. Fig. 6(b) shows that the number of original coarse grains was significantly reduced and that the grains exhibited different orientations after the extrusion deformation degree of the magnesium alloy was increased. This shows that the grain refinement was plain after the Φ10 FE process and that there is no obvious preferred orientation. Fig. 6(c) and (d) show that the grain orientation difference is still large after the FPE processes. Notably, the grown DRXed grains were broken when passing through the extrusion corners, further refining the grain size; reducing the shear force will affect the extent of this grain breakage. Hence, the grain size was larger after 105° FPE than after 90° FPE.

Fig. 7 shows the grain boundary diagrams of the Mg–5Li–3Sn–2Al–1Zn alloy after the hot extrusion processes and the statistical results of the grain boundary orientation difference. The grain

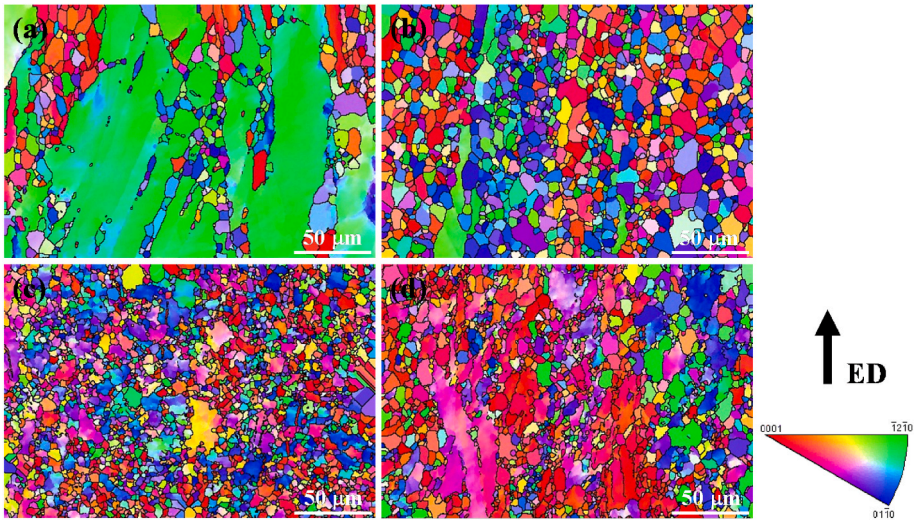

Fig. 6. Orientation maps of the alloys after hot extrusion processes:(a) Φ12 FE, (b) Φ10 FE, (c) 90° FPE, and (d) 105° FPE.

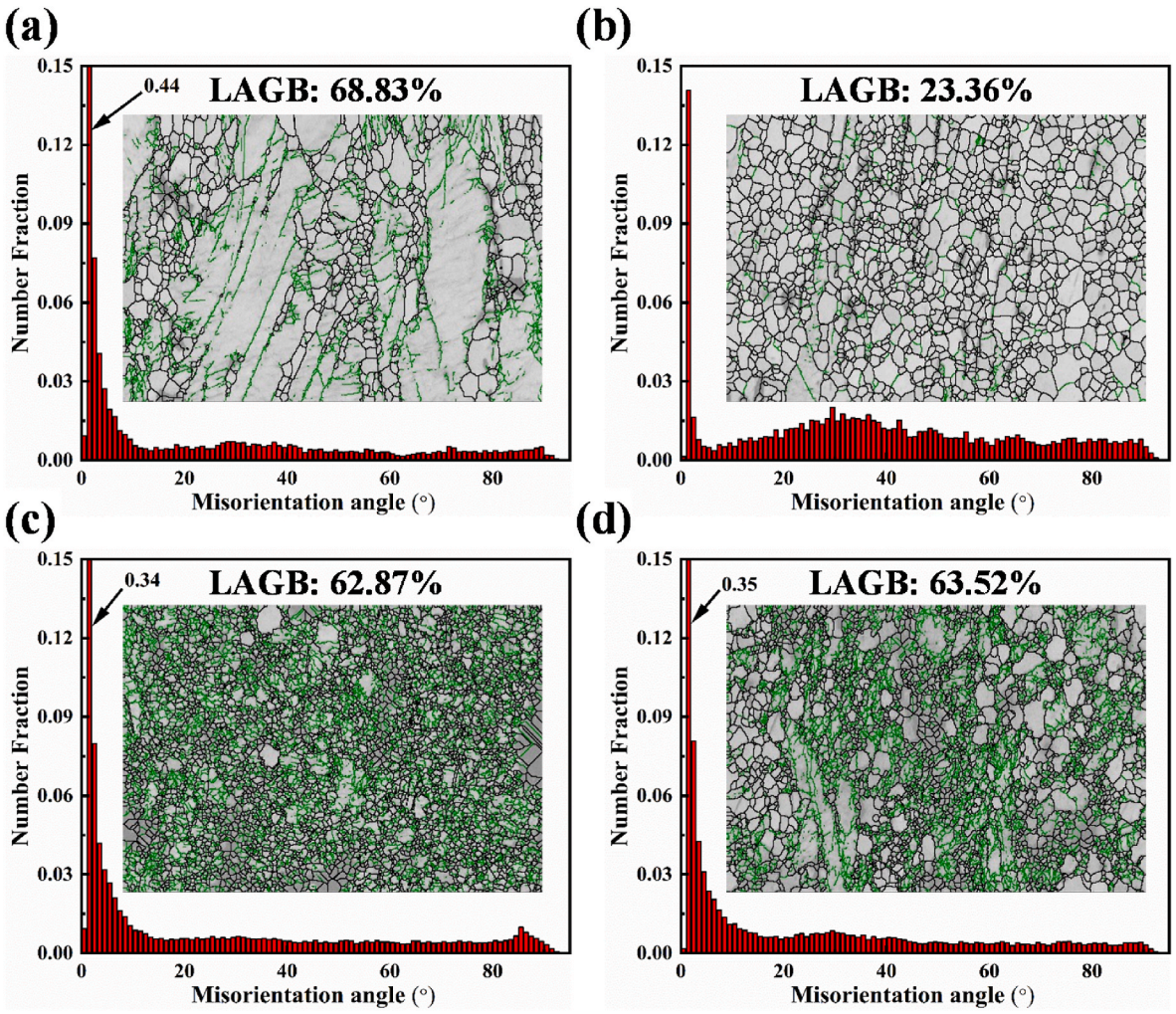

Fig. 7. Grain boundary diagrams and statistical results of the grain boundary orientation difference of the alloys after the hot extrusion processes: (a) Φ12 FE, (b) Φ10 FE, (c) 90° FPE, and (d) 105° FPE.

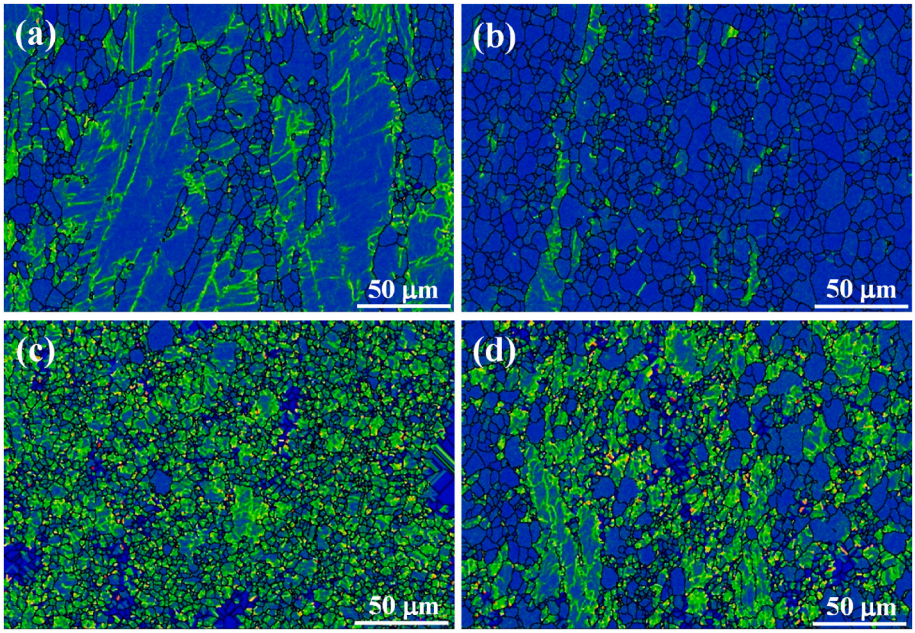

Fig. 8. KAM maps of the alloys after the hot extrusion processes:(a) Φ12 FE, (b) Φ10 FE, (c) 90° FPE, and (d) 105° FPE.

boundary orientation difference between 2° and 5° is the low-angle grain boundary (LAGB), indicated by the green lines, and the grain boundary orientation difference above 15° is the high-angle grain boundary (HAGB), indicated by the black lines. The DRXed grains are grains with an orientation difference above 15°. In Fig. 7(a), after the Φ12 FE process, the LAGBs account for 68.83%, and these LAGBs are distributed around the original un-DRXed grains. In Fig. 7(b), there is a significant decrease in the percentage of LAGBs after the Φ10 FE extrusion process, accounting for 23.36%. With an increase in the extrusion ratio, the corresponding strain increases, resulting in dislocations with high mobility and a significant reduction of the LAGBs, which then transform into HAGBs [32]. With an increase in the plastic deformation degree, more grains experienced dynamic recrystallization, dislocations increased and migrated, the recrystallization of nucleation and growth eliminated the lattice distortion, and grain distribution had increased uniformity. In Fig. 7(c) and (d), the alloy was still distributed with many LAGBs after the FPE processes, but the average grain size was significantly reduced. This phenomenon also illustrates that the DRXed grains were broken under the shear force, and the decrease in the shear force will weaken the degree of grain breakage. In addition, a necklace-like structure can be observed around the deformed grains. This process requires no nucleation and growth stages and is called continuous dynamic recovery and recrystallization (CDRR) [33].

Fig. 8 shows the kernel average misorientation (KAM) maps of the Mg–5Li–3Sn–2Al–1Zn alloy after the hot extrusion processes. The green part of the diagram indicates the dislocation density. The dislocations were mostly distributed inside the deformed grains and around the substructure after the Φ12 FE process (Fig. 8(a)). This is because adding Li increased the stacking fault energy and dynamic recovery (DRV). Under the influence of DRV, the dislocations within the substructure will be rearranged, and dissimilar dislocations will cancel each other, leaving dislocations distributed around and not inside the substructure. However, with the dislocations pile-up and dislocations tangle around the substructure, the stored energy inside the alloy increased rapidly. To release the stored energy, the dislocations transform the sub-grains into deformed grains by slipping and climbing; thus, the dislocation density inside the deformed grains was superior. Fig. 8(b) shows that the dislocation density is reduced due to the large deformation of the Φ10 FE process. When the dislocations are accumulated to a certain degree, DRX nucleation is promoted with continued deformation, and the generated fine DRXed grains will absorb the dislocations and grow. In Fig. 8(c) and (d), the grain size of the alloy is fine, and the grain dislocation density is extremely high when the two shear deformation processes are combined. Moreover, the grains were mainly deformed grains. Since the grown DRXed grains continue to be broken by plastic deformation, an increased amount of deformation increases the lattice deformation energy stored in the material, forming many deformed grains and increasing the nucleation point for recrystallization [34]. Accordingly, the reduced shear deformation induces a decrease in dislocation density while allowing more DRXed grains to be preserved.

Fig. 9 shows the TEM images of the Mg–5Li–3Sn–2Al–1Zn alloy after the hot extrusion processes. In Fig. 9(a), there are only a few dislocations at the center of the coarse grains, and most dislocations appear around the grain boundaries of the coarse grains, which can be judged as the substructure in combination with the analysis of the KAM maps. The substructure transforms into DRXed grains by rotation with the slip of dislocations, which behaves as a typical CDRX feature [35]. From Fig. 9 (b), many LAGBs were distributed at the boundaries of the dislocation-focused zones. During extrusion, these LAGBs will continuously absorb dislocations, gradually transform into HAGBs, and then into DRXed grains. Fig. 9(c) and (d) show the TEM images of the alloy after the FPE processes. The dislocation density is increased when the shear deformation process is compounded, and numerous dislocation pile-up and dislocation tangle can be seen. The <a + c> dislocations in Fig. 9(c) would favor the transformation of LAGBs to HAGBs. The DRXed grain, dislocation pile-up, and substructure can be seen in Fig. 9(d). With the slip of dislocations, the dislocation pile-up would be rearranged to promote the formation of substructures, which would absorb the dislocations and thus increase the grain boundary orientation difference and form HAGBs.

Fig. 10 shows the distribution diagrams of the recrystallized, substructured, and deformed grains of the Mg–5Li–3Sn–2Al–1Zn alloy after the hot extrusion processes. The blue, yellow, and red parts in the diagram indicate the DRXed, substructured, and deformed grains, respectively. Fig. 11 shows the statistical diagrams of the recrystallized, substructured, and deformed grains. The substructure has the maximum percentage, with a value of 54.44% after the Φ12 FE process. Many substructures were associated with the activation of dislocations, suggesting that the Φ12 FE extrusion process activates the dislocation slips [36]. Moreover, the coarse subgrains can act as the nucleation of dynamic recrystallization to grow further [37]. In addition, 80% of the grains in Fig. 11(b) are recrystallized grains, indicating that the alloy

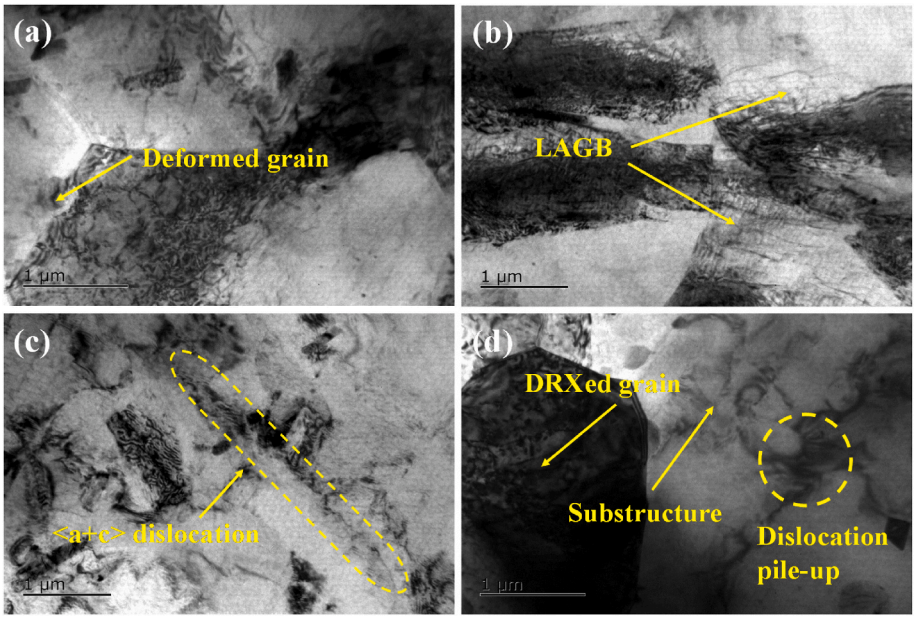

Fig. 9. TEM image of the alloys after hot extrusion processes: (a) Φ12 FE, (b) Φ10 FE,(c) 90° FPE, and (d) 105° FPE.

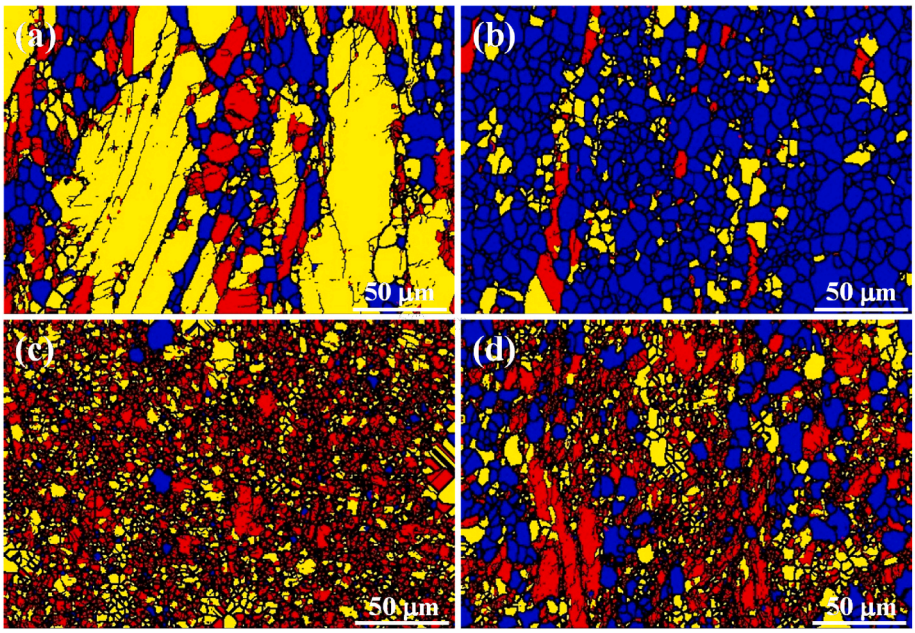

Fig. 10. Distribution diagrams of the recrystallized, substructured, and deformed grains of the alloys after hot extrusion processes: (a) Φ12 FE, (b) Φ10 FE, (c) 90° FPE, and (d) 105° FPE.

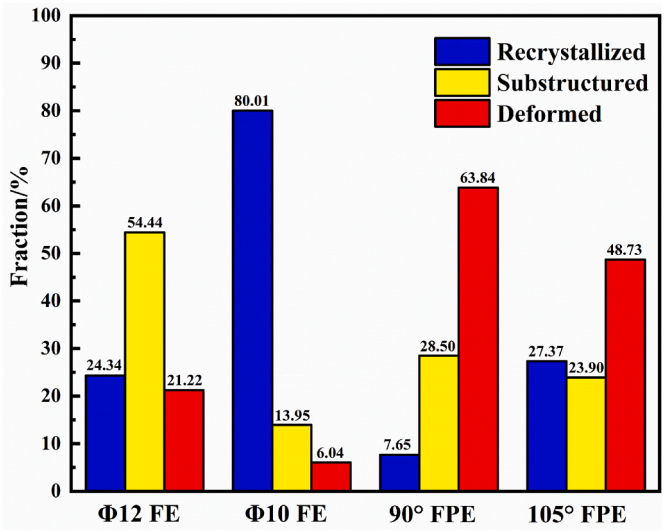

Fig. 11. Statistical diagrams of the recrystallized, substructured, and deformed grains of the alloy after hot extrusion processes: (a) Φ12 FE, (b) Φ10 FE, (c) 90° FPE, and (d) 105° FPE.

experienced significant dynamic recrystallization after the Φ10 FE process. More than half of the grains in Fig. 11(c) are deformed, and nearly a third are substructured, indicating a very small degree of DRX. Consistent with the previous conclusions, most DRXed grains were broken and failed to grow, thus exhibiting deformed grains. In Figs. 11 (d), 48.73% of the grains are deformed grains. Compared with the 90° FPE process, we found that reducing the shear deformation significantly improves the degree of DRX and decreases the proportion of DRXed grains that break.

4.2. Texture evolution during different extrusion processes

Fig. 12 shows the pole figures of the Mg–5Li–3Sn–2Al–1Zn alloy after the hot extrusion processes. In Fig. 12(a), the maximum value of the basal texture intensity is 41.3. This is due to the small range of the EBSD test collection and the large size of the original grains in the collected zones, which makes the values of the measured texture intensity high. In contrast, the maximum value of the basal texture intensity in Fig. 12(b) is 5.56, showing a significant decrease for the following reasons. First, the increased extrusion ratio activates the non-basal slip and weakens the basal texture intensity. Second, the increased extrusion ratio drives the grains to an increased degree of DRX, while the DRXed grains exhibit a random orientation, resulting in a reduced basal texture intensity. In Fig. 12(c) and (d), after two passes of shear deformation processes compound, the DRXed grains break under the influence of shear force, resulting in many deformed grains and an increase in the basal texture intensity [34]. Moreover, the decreased shear deformation, shown in Fig. 12(d), increased the basal texture intensity.

Fig. 13 shows the macrotexture of the Mg–5Li–3Sn–2Al–1Zn alloy after the hot extrusion processes. Comparing Fig. 13(a) and (b), the intensities of both the basal and cylindrical textures of the alloy were significantly reduced after the Φ10 FE process, which is mainly due to the increased degree of DRX caused by the increased extrusion ratio. In Fig. 13(c), the intensity of the cylindrical texture is similar to that of the basal texture after the alloy experienced the 90° FPE process. This indicates that the added two passes of shear deformation caused the grains to rotate during extrusion, with varying grain orientations and a significant weakening of the basal texture [38]. In Fig. 13(d), the alloy exhibits $<10\bar{1}0>\|$ED-preferred orientation after the 105° FPE process, and the decrease in shear deformation reduces the basal texture intensity.

4.3. Effects of extrusion processes on the elongation of the Mg–5Li–3Sn–2Al–1Zn alloy

According to the above, the hot extrusion process is imperative in grain refinement. The Hall–Petch relationship states that a reduction in grain size benefits the mechanical properties of the alloy [39,40]. Combining Table 2 and Fig. 5(b), we found that after increasing the extrusion ratio, the TYS and UTS of the alloy slightly decreased, and the EL slightly increased. This is due to the higher degree of DRX in the Φ10 FE process compared to the Φ12 FE process and the fact that the DRXed grains have some weakening effect on the basal texture, hence increasing the EL [41]. As for the two FPE processes, we found that

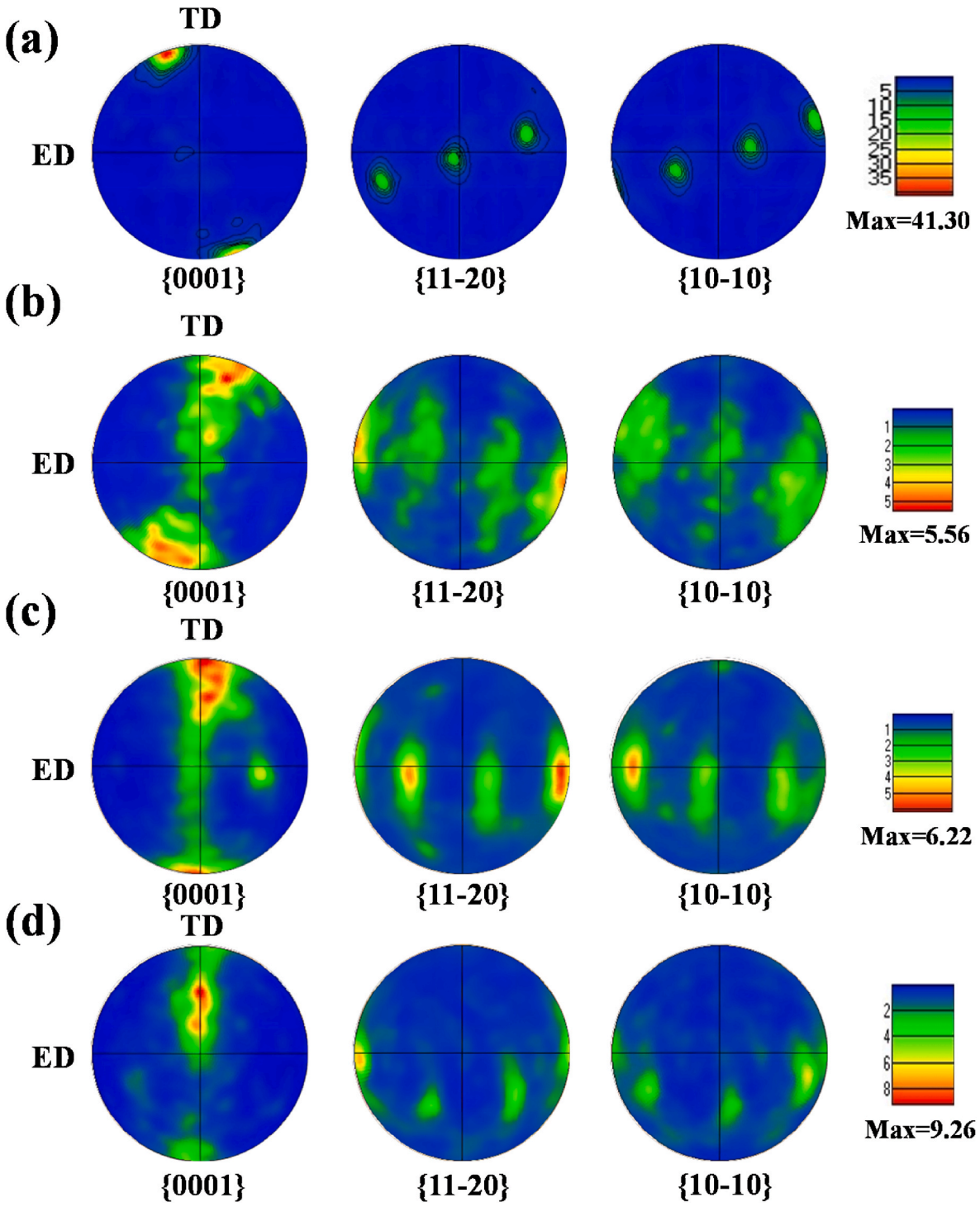

Fig. 12. Pole figures of the alloys after the hot extrusion processes: (a) Φ12 FE, (b) Φ10 FE,(c) 90° FPE, and (d) 105° FPE.

although there is no change in the extrusion ratio, the difference in the extrusion process also influences the mechanical properties of the alloy. Combined with Table 2 and Fig. 5(b), the FE processes have a slight advantage in improving the TYS and UTS of the alloy, while the FPE processes are beneficial in improving the EL of the alloy. Hence, the two additional shear deformation processes positively affected the alloy properties, and the plasticity of the alloy increased significantly after the 105° FPE process. The EL of the alloy increased by 134.4% compared to the as-homogeneous alloy, while the TYS and UTS of the alloy also increased by 61.8% and 44.4%, respectively. The significant increase in alloy plasticity is related to the grain size and weakening of the alloy basal texture. The grain size of the alloy after the 105° FPE process is uniform and fine. With more grains per unit volume, the area of grain boundaries also increases, which is beneficial for plastic deformation to be dispersed in more grains and induces an improvement in the EL of the alloy [42]. In addition, the improvement of the EL may be related to other factors, such as the extent of the fine grain zone, the uniformity of the microstructure, internal stresses, dislocation density, and metal formation processes [38,43].

Based on the data of the mechanical properties of typical extruded magnesium alloys in Table 3, the Mg–Sn–Al–Zn system alloys without Li possess high TYS and UTS, showing that Sn, Al, and Zn have an excellent

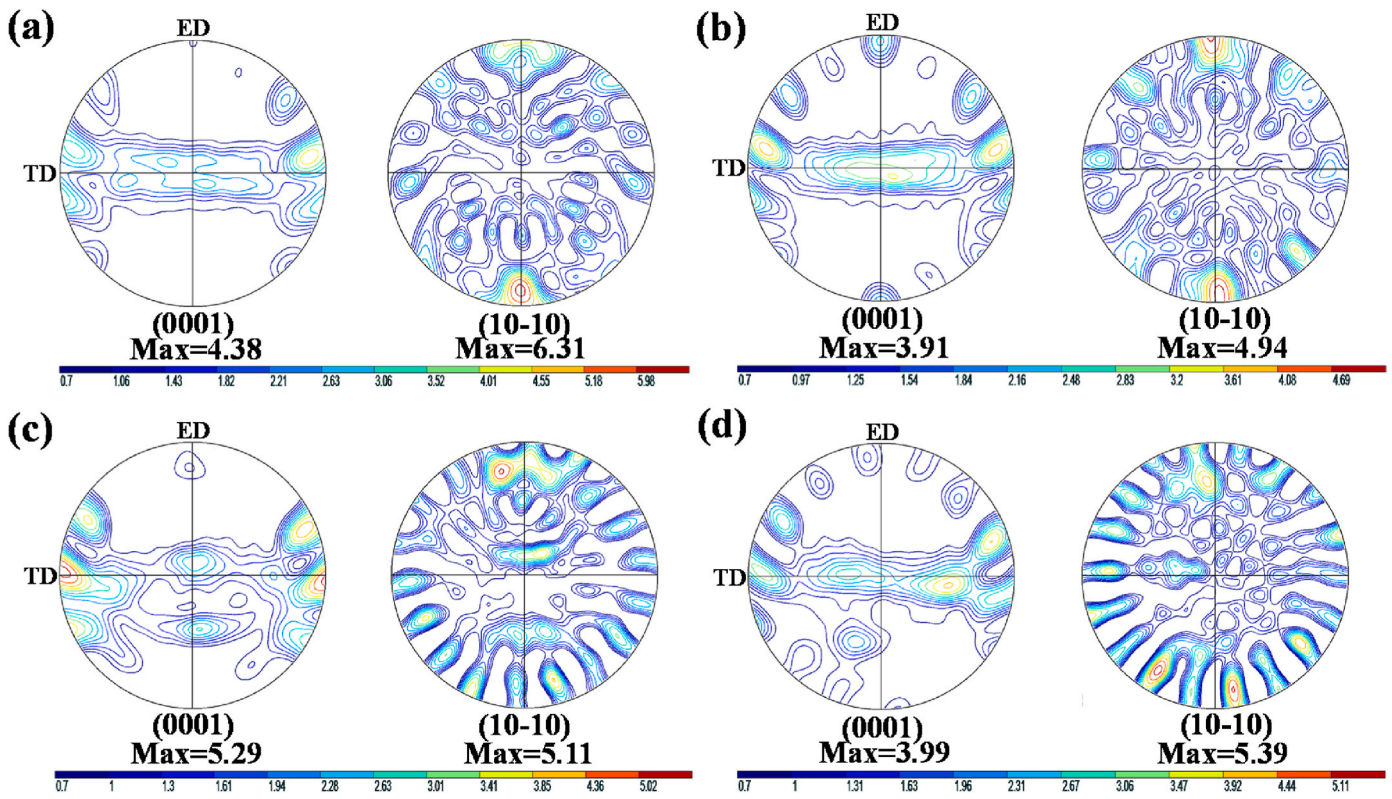

Fig. 13. Macrotexture of the alloys after hot extrusion processes: (a) Φ12 FE, (b) Φ10 FE,(c) 90° FPE, and (d) 105° FPE.

Table 3
Mechanical properties of the as-extruded Mg–5Li–3Sn–2Al–1Zn alloy and the typical magnesium alloys under the as-extrusion addition.

Alloy composition	TYS (MPa)	UTS (MPa)	EL (%)	Ref.
Mg–7Sn–1Al–1Zn	194	271	13.4	[44]
Mg–9.8Sn–3.0Al–1.23Zn	319	358	6.1	[45]
Mg–5Li	77	159	17.0	[46]
Mg–5Li–3Al	143	233	18.2	[12]
Mg–5Li–3Al–2Zn	150.8	284.1	16.9	[47]
Mg–7Li–2Al-1.5Sn	250	324	11.9	[48]
Mg–8Li	106	141	19	[26]
Mg–8Li–2Al	113	180	16	[26]
Mg–8Li–3Al	164	214	20.9	[12]
Mg–8Li–1Al-0.5Sn	240	322	11	[8]
Mg–11Li–3Zn	124.5	137.7	56.1	[24]
Mg–5Li–3Sn–2Al–1Zn	178	270	21.03	This work

strengthening effect, which makes the plasticity of the magnesium alloy reduce sharply [44,45]. However, the plasticity of the Mg–Li alloy is excellent. An increased Li content improves plasticity, but the strength is particularly low [26,46]. Hence, adding these elements to Mg–Li alloys will reduce the disadvantage of poor strength and make Mg–Li-based alloys possess high strength or good ductility [12,26,47,48]. In this work, the alloy composition was designed rationally to achieve low alloying, and the extrusion process was optimized to considerably improve the comprehensive mechanical properties of the Mg–Li alloy. However, the mechanical properties of the Mg–Li alloy in this work are still expected to be further improved by fully utilizing alloying and fine-grained strengthening and thermomechanical processing.

The SEM morphology of the tensile fracture surfaces of the Mg–5Li–3Sn–2Al–1Zn alloy specimens after the hot extrusion processes are shown in Fig. 14. The tensile fracture surfaces were composed of small dimples and fewer crack sources. This result is consistent with that reported by Li [46], where the size of the microcracks caused by the slip band of the Mg–5Li alloy was small, and the alloy experienced relatively uniform plastic deformation. This phenomenon shows that hot extrusion processes can effectively eliminate the aggregation of second-phase precipitation of casting defects, significantly increasing the plasticity of the alloy, consistent with the above results for tensile plasticity [49]. In Fig. 14(a) and (b), after the FE processes, there are few dimples and many cleavage surfaces in the tensile fracture of the specimen, and many precipitated particles are dispersed in the matrix as particle bands. This can relieve local stress concentrations around the particles, exhibiting a mixed fracture mode of ductile and brittle fractures. In Fig. 14(b), the tensile fracture surface of the specimen is smooth after the Φ10 FE process, and many dimples exist around the tear ridges. The plasticity of the alloy is further improved compared to the Φ12 FE process, but it still belongs to the mixed fracture mode of brittle and ductile fractures. Fig. 14(c) shows the tensile fracture of the specimen after the 90° FPE process, where many dimples exist on the surface of the alloy, indicating that the alloy experienced a significant deformation during the tensile process with good plastic deformation properties. In addition, some cleavage surfaces and steps can be observed on the alloy surface, indicating that a cleavage fracture has also occurred in the alloy. This belongs to the mixed fracture mode of brittle and ductile fractures, but ductile fracture dominates. Fig. 14(d) shows the tensile fracture of the specimen after the 105° FPE process. The diagram shows that the number of dimples on the fracture surface is increasingly significant, indicating that the plasticity of the alloy is better after the 105° FPE process, and the fracture mechanism is dominated by the ductile fracture.

5. Conclusion

Four different hot extrusion processes were conducted for the homogeneous Mg–5Li–3Sn–2Al–1Zn alloy. After each hot extrusion process, the alloy microstructure was observed, and tensile tests were performed at room temperature. Consequently, the following conclusions were obtained.

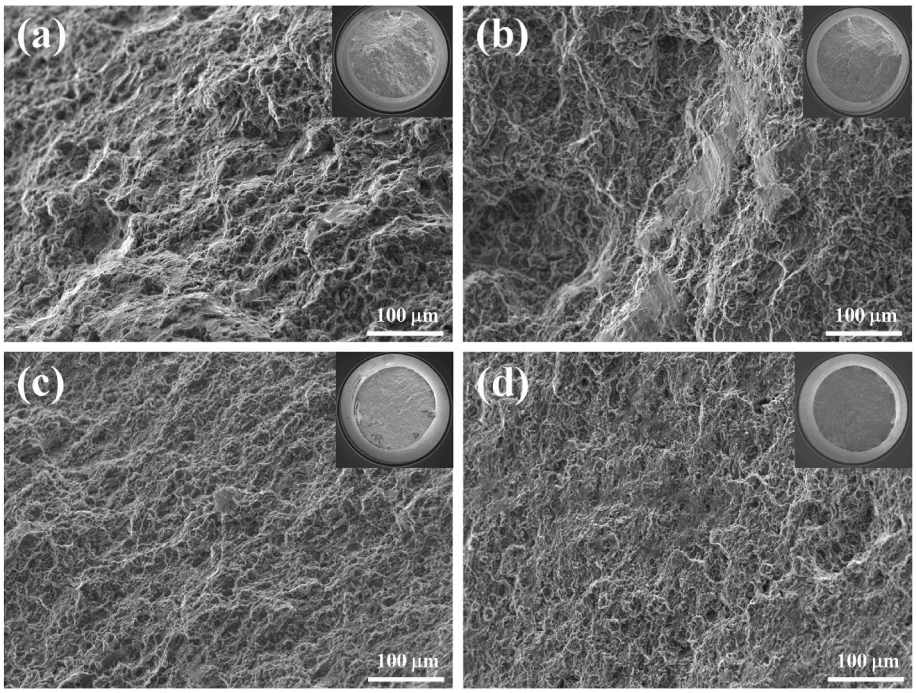

Fig. 14. SEM morphology of the tensile fracture surfaces of the alloy specimens after hot extrusion processes: (a) Φ12 FE, (b) Φ10 FE, (c) 90° FPE, and (d) 105° FPE.

(1) Three phases, α-Mg, Mg_2Sn, and Li_2MgSn, were observed in the Mg–5Li –3Sn–2Al–1Zn alloy after the homogenization treatment at 400 °C for 24 h. The four hot extrusion processes did not change the precipitation phases of the Mg–5Li–3Sn–2Al–1Zn alloy. After the hot extrusion processes, the precipitated phases were fragmented and distributed in the alloy, and the degree of fragmentation increased after the FPE processes.

(2) Dynamic recrystallization occurred during the hot extrusion processes, and the grains were significantly finer than those of the as-homogeneous alloy. Additionally, the FPE processes showed superior grain refinement. After the 105° FPE process, the Mg–5Li–3Sn–2Al–1Zn alloy had a fine and uniform microstructure, with an average grain size of 3.56 μm. Furthermore, the basal texture was significantly weakened, which is attributed to the addition of two passes of the 105° ECAP processes.

(3) The TYS, UTS, and EL of the Mg–5Li–3Sn–2Al–1Zn alloy increased after the hot extrusion processes. The alloy showed optimal mechanical properties after the 105° FPE process. In addition, the EL is 21.03% without the loss of TYS and UTS, which is an increase of 134.4% compared to that of the as-homogeneous alloy. The significant increase in plasticity is due to the weakening of the basal texture and grain refinement.

(4) The fracture mechanism of the alloy after the hot extrusion processes is a combination of ductile and brittle fractures. The difference is that the alloy shows excellent plastic deformation after the FPE processes. There are increased dimples, and ductile fracture plays a major role. The plasticity of the alloy is optimal after the 105° FPE process.

CRediT authorship contribution statement

Yuhang Guo: Conceptualization, Methodology, Formal analysis, Funding acquisition, Project administration, Writing – review & editing. **Xuancheng He:** Methodology, Software, Resources, Data curation, Writing – original draft, Writing – review & editing. **Yibo Dai:** Methodology, Software, Investigation, Validation. **Qianhao Zang:** Methodology, Visualization, Supervision. **Xuguang Dong:** Methodology, Resources, Data curation. **Zhenya Zhang:** Methodology, Resources, Data curation.

Declaration of competing interest

The authors declare that they have no known competing financial interests or personal relationships that could have appeared to influence the work reported in this paper.

Data availability

Data will be made available on request.

Acknowledgments

This work was supported financially by the Doctoral Research Start-Up Fund of the Jiangsu University of Science and Technology (No.1062932101). The authors are grateful for the financial support from the Guangdong Basic and Applied Basic Research Foundation (No. 2020A1515110394).

References

[1] J.F. Song, J. Chen, X.M. Xiong, X.D. Peng, D.L. Chen, F.S. Pan, Research advances of magnesium and magnesium alloys worldwide in 2021, J. Magnes. Alloys. 10 (2022) 863–898, https://doi.org/10.1016/j.jma.2022.04.001.

[2] T.C. Chang, J.Y. Wang, C.L. Chu, S. Lee, Mechanical properties and microstructures of various Mg-Li alloys, Mater. Lett. 60 (2006) 3272–3276, https://doi.org/10.1016/j.matlet.2006.03.052.

[3] J. Li, L. Jin, F.H. Wang, S. Dong, J. Dong, Effect of phase morphology on microscopic deformation behavior of Mg-Li-Gd dual-phase alloys, Mater. Sci. Eng. 809 (2021), 140871, https://doi.org/10.1016/j.msea.2021.140871.

[4] D.K. Xu, B.J. Wang, C.Q. Li, T.T. Zu, E.H. Han, Effect of icosahedral phase on the thermal stability and ageing response of a duplex structured Mg-Li alloy, Mater. Des. 69 (2015) 124–129, https://doi.org/10.1016/j.matdes.2014.12.057.

[5] R. Wu, Y. Yan, G. Wang, L.E. Murr, W. Han, Z. Zhang, M. Zhang, Recent progress in magnesium-lithium alloys, Int. Mater. Rev. 60 (2015) 65–100, https://doi.org/10.1179/1743280414Y.0000000044.

[6] J. Zhao, Z.Q. Li, W.C. Liu, J. Zhang, L. Zhang, Y. Tian, G.H. Wu, Influence of heat treatment on microstructure and mechanical properties of as-cast Mg-8Li-3Al-2Zn-xY alloy with duplex structure, Mater. Sci. Eng. 669 (2016) 87–94, https://doi.org/10.1016/j.msea.2016.05.085.

[7] S.H. Lv, X.L. Lv, F.Z. Meng, Y.W. Li, Q. Duan, Q. Yang, Microstructures and mechanical properties of a hot-extruded Mg-8Ho-0.6Zn-0.5Zr alloy, J. Alloys Compd. 774 (2019) 926–938, https://doi.org/10.1016/j.jallcom.2018.09.375.
[8] X.S. Fu, Y. Yang, J.W. Hu, J.F. Su, X.P. Zhang, X.D. Peng, Microstructure and mechanical properties of as-cast and extruded Mg-8Li-1Al-0.5Sn alloy, Mater. Sci. Eng. 709 (2018) 247–253, https://doi.org/10.1016/j.msea.2017.10.036.
[9] J.S. Miao, W.H. Sun, A.D. Klarner, A.A. Luo, Interphase boundary segregation of silver and enhanced precipitation of Mg17Al12 Phase in a Mg-Al-Sn-Ag alloy, Scripta Mater. 154 (2018) 192–196, https://doi.org/10.1016/j.scriptamat.2018.05.047.
[10] K.N. Braszczynska-Malik, Effect of high-pressure die casting on structure and properties of Mg-5Al-0.4Mn-xRE (x=1, 3 and 5 wt%) experimental alloys, J. Alloys Compd. 694 (2017) 841–847, https://doi.org/10.1016/j.jallcom.2016.10.033.
[11] J. Wang, J. Meng, D. Zhang, D.X. Tang, Effect of Y for enhanced age hardening response and mechanical properties of Mg-Gd-Y-Zr alloys, Mater. Sci. Eng. 456 (2007) 78–84, https://doi.org/10.1016/j.msea.2006.11.096.
[12] Y.H. Kim, J.H. Kim, H.S. Yu, J.W. Choi, H.T. Son, Microstructure and mechanical properties of Mg-xLi-3Al-1Sn-0.4Mn alloys (x=5, 8 and 11 wt%), J. Alloys Compd. 583 (2014) 15–20, https://doi.org/10.1016/j.jallcom.2013.08.154.
[13] H. Ji, G.H. Wu, W.C. Liu, X.L. Liang, G.L. Liao, D.H. Ding, Microstructure characterization and mechanical properties of the as-cast and as-extruded Mg-xLi-5Zn-0.5Er (x=8, 10 and 12 wt%) alloys, Mater. Char. 159 (2020), 110008, https://doi.org/10.1016/j.matchar.2019.110008.
[14] X.Y. Chen, Y. Zhang, M.Q. Cong, Y.L. Lu, X.P. Li, Effect of Sn content on microstructure and tensile properties of as-cast and as-extruded Mg-8Li-3A1-(1,2,3)Sn alloys, Trans. Nonferrous Metals Soc. China 30 (2020) 2079–2089, https://doi.org/10.1016/S1003-6326(20)65362-6.
[15] W.Q. Xu, N. Birbilis, G. Sha, Y. Wang, J.E. Daniels, Y. Xiao, M. Ferry, A high-specific-strength and corrosion-resistant magnesium alloy, Nat. Mater. 14 (2015) 1229–1235, https://doi.org/10.1038/nmat4435.
[16] J. Zhang, Y. Zhang, G.H. Wu, W.C. Liu, L. Zhang, W.J. Ding, Microstructure and mechanical properties of as-cast and extruded Mg-8Li-3Al-2Zn-0.5Nd alloy, Mater. Sci. Eng. 621 (2015) 198–203, https://doi.org/10.1016/j.msea.2014.10.076.
[17] F.P. Fei, Z.K. Qu, R.Z. Wu, Microstructure and hardness of Mg-9Li-6Al-xLa (x=0, 2, 5) alloys during solid solution treatment, Mater. Sci. Eng. 625 (2015) 169–176, https://doi.org/10.1016/j.msea.2014.12.014.
[18] C.Q. Liu, H.W. Chen, J.F. Nie, Interphase boundary segregation of Zn in Mg-Sn-Zn alloys, Scripta Mater. 123 (2016) 5–8, https://doi.org/10.1016/j.scriptamat.2016.05.035.
[19] S.H. Park, J.G. Jung, J.H. Yoon, B.S. You, Influence of Sn addition on the microstructure and mechanical properties of extruded Mg-8Al-2Zn alloy, Mater. Sci. Eng. 626 (2015) 128–135, https://doi.org/10.1016/j.msea.2014.12.039.
[20] M. Zhang, W.Z. Zhang, G.Z. Zhu, The morphology and crystallography of polygonal Mg2Sn precipitates in a Mg-Sn-Mn-Si alloy, Scripta Mater. 59 (2008) 866–869, https://doi.org/10.1016/j.scriptamat.2008.06.033.
[21] Q.X. Shi, L.P. Bian, W. Liang, Z.Q. Chen, F.Q. Yang, Y.D. Wang, Effects of adding Al-Si eutectic alloy and hot rolling on microstructures and mechanical behavior of Mg-8Li alloys, J. Alloys Compd. 631 (2015) 129–132, https://doi.org/10.1016/j.jallcom.2015.01.094.
[22] Z. Zhang, J.H. Zhang, J. Wang, Z.H. Li, J.S. Xie, S.J. Liu, K. Guan, R.Z. Wu, Toward the development of Mg alloys with simultaneously improved strength and ductility by refining grain size via the deformation process, Int. J. Miner. Metall. Mater. 28 (2021) 30–45, https://doi.org/10.1007/s12613-020-2190-1.
[23] Y.H. Sun, R.C. Wang, C.Q. Peng, Y. Feng, Effects of Sn and Y on the microstructure, texture, and mechanical properties of as-extruded Mg-5Li-3Al-2Zn alloy, Mater. Sci. Eng. 733 (2018) 429–439, https://doi.org/10.1016/j.msea.2018.05.030.
[24] H.T. Son, Y.H. Kim, D.W. Kim, J.H. Kim, H.S. Yu, Effects of Li addition on the microstructure and mechanical properties of Mg-3Zn-1Sn-0.4Mn based alloys, J. Alloys Compd. 564 (2013) 130–137, https://doi.org/10.1016/j.jallcom.2013.02.157.
[25] Y. Tang, Q.C. Le, W.T. Jia, L. Fu, X. Liu, J.Z. Cui, Microstructure evolution and strengthening mechanism study of Mg-Li alloys during deformation and heat treatment, Mater. Sci. Eng. 704 (2017) 344–359, https://doi.org/10.1016/j.msea.2017.08.043.
[26] B.S. Pugazhendhi, A. Kar, K. Sinnaeruvadi, S. Suwas, Effect of aluminium on microstructure, mechanical property and texture evolution of dual phase Mg-8Li alloy in different processing conditions, Arch. Civ. Mech. Eng. 18 (2018) 1332–1344, https://doi.org/10.1016/j.acme.2018.04.001.
[27] J. Guo, L.L. Chang, Y.R. Zhao, Y.P. Jin, Effect of Sn and Y addition on the microstructural evolution and mechanical properties of hot-extruded Mg-9Li-3Al alloy, Mater. Char. 148 (2019) 35–42, https://doi.org/10.1016/j.matchar.2018.11.030.
[28] Z.R. Zeng, N. Stanford, C.H.J. Davies, J.F. Nie, N. Birbilis, Magnesium extrusion alloys: a review of developments and prospects, Int. Mater. Rev. 64 (2019) 27–62, https://doi.org/10.1080/09506608.2017.1421439.
[29] D.H. Lee, G.M. Lee, S.H. Park, Difference in extrusion temperature dependences of microstructure and mechanical properties between extruded AZ61 and AZ91 alloys, J. Magnes. Alloys (2022), https://doi.org/10.1016/j.jma.2022.05.015.
[30] L.B. Tong, J.H. Chu, Z.H. Jiang, S. Kamado, M.Y. Zheng, Ultra-fine grained Mg-Zn-Ca-Mn alloy with simultaneously improved strength and ductility processed by equal channel angular pressing, J. Alloys Compd. 785 (2019) 410–421, https://doi.org/10.1016/j.jallcom.2019.01.181.
[31] L.B. Tong, J.H. Chu, W.T. Sun, Z.H. Jiang, D.N. Zou, K.S. Wang, S. Kamado, M. Y. Zheng, Development of high-performance Mg-Zn-Ca-Mn alloy via an extrusion process at relatively low temperature, J. Alloys Compd. 825 (2020), 153942, https://doi.org/10.1016/j.jallcom.2020.153942.
[32] T.S. Zhao, Y.B. Hu, C. Zhang, B. He, T.X. Zheng, A.T. Tang, F.S. Pan, Influence of extrusion conditions on microstructure and mechanical properties of Mg-2Gd-0.3Zr magnesium alloy, J. Magnes. Alloys. 10 (2022) 387–399, https://doi.org/10.1016/j.jma.2020.06.019.
[33] P.C. Gautam, S. Biswas, On the possibility to reduce ECAP deformation temperature in magnesium: deformation behaviour, dynamic recrystallization and mechanical properties, Mater. Sci. Eng. 812 (2021), 141103, https://doi.org/10.1016/j.msea.2021.141103.
[34] X.Q. Li, L. Ren, Q.C. Le, L. Bao, P.P. Jin, P. Wang, C.L. Cheng, X. Zhou, C.L. Hu, Reducing the yield asymmetry in Mg-5Li-3Al-2Zn alloy by hot-extrusion and multi-pass rolling, J. Magnes. Alloys 9 (2021) 937–949, https://doi.org/10.1016/j.jma.2020.06.015.
[35] W.L. Cheng, Y. Bai, S.C. Ma, L.F. Wang, H.X. Wang, H. Yu, Hot deformation behavior and workability characteristic of a fine-grained Mg-8Sn-2Zn-2Al alloy with processing map, J. Mater. Sci. Technol. 35 (2019) 1198–1209, https://doi.org/10.1016/j.jmst.2018.12.001.
[36] L.R. Xiao, X.F. Chen, K. Wei, Y. Liu, D.D. Yin, Z.H. Hu, H. Zhou, Y.T. Zhu, Effect of dislocation configuration on Ag segregation in subgrain boundary of a Mg-Ag alloy, Scripta Mater. 191 (2021) 219–224, https://doi.org/10.1016/j.scriptamat.2020.08.040.
[37] H. Ji, G.H. Wu, W.C. Liu, J.W. Sun, W.J. Ding, Role of extrusion temperature on the microstructure evolution and tensile properties of an ultralight Mg-Li-Zn-Er alloy, J. Alloys Compd. 876 (2021), 160181, https://doi.org/10.1016/j.jallcom.2021.160181.
[38] H.J. Hu, Y.L. Ying, Z.W. Ou, X.Q. Wang, Comparisons of microstructures and texture and mechanical properties of magnesium alloy fabricated by compound extrusion and direct extrusion, Mater. Sci. Eng. 695 (2017) 360–366, https://doi.org/10.1016/j.msea.2017.03.103.
[39] B.N. Du, Z.Y. Hu, L.Y. Sheng, D.K. Xu, Y.X. Qiao, B.J. Wang, J. Wang, Y.F. Zheng, T. F. Xi, Microstructural characteristics and mechanical properties of the hot extruded Mg-Zn-Y-Nd alloys, J. Mater. Sci. Technol. 60 (2021) 44–55, https://doi.org/10.1016/j.jmst.2020.05.021.
[40] H.H. Yu, Y.C. Xin, M.Y. Wang, Q. Liu, Hall-Petch relationship in Mg alloys: a review, J. Mater. Sci. Technol. 34 (2018) 248–256, https://doi.org/10.1016/j.jmst.2017.07.022.
[41] W. Yang, G.F. Quan, B. Ji, Y.F. Wan, H. Zhou, J. Zheng, D.D. Yin, Effect of Y content and equal channel angular pressing on the microstructure, texture and mechanical property of extruded Mg-Y alloys, J. Magnes. Alloys. 10 (2022) 195–208, https://doi.org/10.1016/j.jma.2020.08.021.
[42] N. Zhou, Z.Y. Zhang, J. Dong, L. Jin, W.J. Ding, High ductility of a Mg-Y-Ca alloy via extrusion, Mater. Sci. Eng. 560 (2013) 103–110, https://doi.org/10.1016/j.msea.2012.09.042.
[43] J.Y. Zhang, Z.X. Kang, L.L. Zhou, Microstructure evolution and mechanical properties of Mg-Gd-Nd-Zn-Zr alloy processed by equal channel angular pressing, Mater. Sci. Eng. 647 (2015) 184–190, https://doi.org/10.1016/j.msea.2015.09.005.
[44] S.H. Park, S.H. Kim, H.S. Kim, J.H. Yoon, B.S. You, High-speed indirect extrusion of Mg-Sn-Al-Zn alloy and its influence on microstructure and mechanical properties, J. Alloys Compd. 667 (2016) 170–177, https://doi.org/10.1016/j.jallcom.2016.01.163.
[45] F.R. Elsayed, T.T. Sasaki, T. Ohkubo, H. Takahashi, S.W. Xu, S. Kamado, K. Hono, Effect of extrusion conditions on microstructure and mechanical properties of microalloyed Mg-Sn-Al-Zn alloys, Mater. Sci. Eng. 588 (2013) 318–328, https://doi.org/10.1016/j.msea.2013.09.050.
[46] C.Q. Li, Y.B. He, H.P. Huang, Effect of lithium content on the mechanical and corrosion behaviors of HCP binary Mg-Li alloys, J. Magnes. Alloys. 9 (2021) 569–580, https://doi.org/10.1016/j.jma.2020.02.022.
[47] X.Q. Li, C.L. Cheng, Q.C. Le, X. Zhou, Q.Y. Liao, X.R. Chen, Y.H. Jia, P. Wang, Ex-situ EBSD analysis of yield asymmetry, texture and twinning development in Mg-5Li-3Al-2Zn alloy during tensile and compressive deformation, J. Alloys Compd. 805 (2019) 947–956, https://doi.org/10.1016/j.jallcom.2019.07.099.
[48] G. Zhou, Y. Yang, H.Z. Zhang, F.P. Hua, X.P. Zhang, C. Wend, W.D. Xie, B. Jiang, X. D. Peng, F.S. Pan, Microstructure and strengthening mechanism of hot-extruded ultralight Mg-Li-Al-Sn alloys with high strength, J. Mater. Sci. Technol. 103 (2022) 186–196, https://doi.org/10.1016/j.jmst.2021.07.009.
[49] S. Feng, W.C. Liu, J. Zhao, G.H. Wu, H.H. Zhang, W.J. Ding, Effect of extrusion ratio on microstructure and mechanical properties of Mg-8Li-3Al-2Zn-0.5Y alloy with duplex structure, Mater. Sci. Eng. 692 (2017) 9–16, https://doi.org/10.1016/j.msea.2017.03.059.